


Direct Measurement of Electrically Modulated Far-Field Thermal Infrared Emission and its Dynamics

Xiu Liu, Hakan Salihoglu, Xiao Luo, Zexiao Wang, Hyeong Seok Yun[✉], Lin Jing, Bowen Yu, and Sheng Shen*

Department of Mechanical Engineering, Carnegie Mellon University, Pittsburgh, Pennsylvania 15213, USA

 (Received 4 October 2022; revised 11 November 2022; accepted 15 February 2023; published 13 March 2023)

Direct measurements of far-field thermal infrared emission become increasingly useful because conventional indirect methods are limited or even unfeasible to characterize state-of-the-art thermal devices with engineered spectra, directionalities, and polarizations. The direct collection of the weak far-field emission from nanoscale infrared devices is also challenging because of their tiny footprints and the relatively large background radiation noises from surroundings. Here, we demonstrate a microscopic lock-in Fourier transform infrared spectrometer (FTIR) system that realizes significant improvement in SNR by combining a microscope and a lock-in amplifier with a FTIR. The lock-in FTIR is ultrasensitive, with a specific detectivity 10^6 times higher than commercial ones, to overcome the optical loss and background noise during the emission light collection. Based on an analytical model of the full signal-detection process, we first employ the combination of the global heating and modulated Joule heating to maximize the potential of our system for noise reduction. Our findings show that, compared to previous studies, more than 3 times lower temperatures are sufficient to generate a measurable signal. Under a heating temperature of around 125°C , we can achieve a SNR of about 23.7, which is far above the true-signal-threshold (SNR of about 3.0). Furthermore, the system can respond fast enough to record spectral-resolved dynamics of microdevices in the frequency domain. The system together with the analytical signal processing can be beneficial for next-generation thermal infrared material and device development, facilitating their applications in lighting, sensing, imaging, and energy harvesting at a small scale.

DOI: [10.1103/PhysRevApplied.19.034040](https://doi.org/10.1103/PhysRevApplied.19.034040)

I. INTRODUCTION

Thermal emission from an object with a finite temperature can be exploited as an infrared fingerprint in extracting material properties and used to measure temperature distributions based on Stefan-Boltzmann's law. Thermal radiation characteristics of bulk materials are typically isotropic, diffuse, and incoherent. With the advent of nanotechnology, thermal infrared microdevices enable versatile functionalities to control emission spectra [1–5], directionalities [6], polarizations [7,8], and power efficiencies [9–11], thus opening opportunities for applications in lighting, sensing, imaging, and energy harvesting [12–17]. The key for these applications is to develop accurate measurement techniques for characterizing thermal emission features of materials and devices. Conventional characterization techniques bear inherent limitations [18,19]. An indirect reflectance and transmittance method that relies on Kirchhoff's law for emissivity measurement can be unreliable for highly scattering or absorptive samples. Moreover, violation of Kirchhoff's law under nonequilibrium or nonreciprocal conditions [20–22] leaves a direct

emission measurement as the only method to obtain thermal emission properties. However, it becomes increasingly challenging to directly collect the weak radiation from miniaturized and compact devices with small footprints, which is usually comparable with ambient thermal noises. Hence, a technique with a proper noise reduction is highly desired for increasing the SNR in thermal emission measurements.

Several techniques have been employed to increase SNR. Intense global heating increases emission signals but gradually becomes impractical, since microdevices can be damaged at a high temperature or contain temperature-sensitive materials [23,24]. Some applications do manage to obtain direct emission under low temperatures [18,25], although typically a large emitting area is needed. Coupling a lock-in amplifier (LIA) to a Fourier transform infrared spectrometer (FTIR) can filter out noises in near-field thermal radiation measurements with a modulated dithering tip [26–28]. The LIA-based noise reduction for far-field emission relies on driving a piezoelectric stage displacing the emitter periodically at 20 Hz [29]. Such a slow spatial modulation, however, still incurs the $1/f$ noise to some extent. A recent work directly measures emission spectra of a device based on a 10 - kHz electrical

*sshens1@cmu.edu

modulation, which necessitates a full-wave rectified cosine wave of far-field emission with a 20 - kHz reference frequency for LIA [30]. Nevertheless, thorough analyses of modulated thermal infrared signals and their underlying physics are still lacking.

Achieving a fast modulation also allows us to characterize the dynamics of thermal emission. Recently, various thermal infrared devices have been employed to achieve rapid modulation of thermal emission with a speed up to GHz level [30–37]. The typical method for characterizing the modulation speed of thermal emission is to measure the total emission power, which is not applicable for several modulation mechanisms, including peak shift for emission resonance tuning [4,32,33], spectrum variation for chemical sensing [38,39], etc. The technique to simultaneously monitor spectra and dynamics of thermal infrared emission is particularly beneficial for material and device exploration.

In this work, we demonstrate a microscopic lock-in FTIR system to directly measure the far-field thermal emission from an electrically modulated microdevice. To reduce the optical loss, a microscope is used to simultaneously locate the emission active region and extract the modulated thermal infrared signal to a FTIR. A LIA then demodulates the signal collected by the FTIR detector to significantly reduce optical and electrical noises during the measurement. We develop an equivalent thermal circuit model for the microdevice and exploit the model to elucidate the full signal-detection process. We also employ the combination of the Joule and global heating to increase the SNR, which results in a more than threefold reduction in heating temperatures to obtain a measurable signal comparable to the previous studies [23,24]. Under a heating temperature of around 125 °C, we can achieve a SNR of about 23.7, which is far above the true-signal-threshold (SNR of about 3.0) [40]. Furthermore, the microscopic lock-in FTIR enables fast response to a high modulation frequency.

II. EXPERIMENTAL METHOD AND SIGNAL-DETECTION MODEL

In our experimental schematic shown in Fig. 1(a), a device under test (DUT) is globally heated up to a reference temperature T_0 by a heating stage and then electrically modulated by a voltage $V(t)$ controlled by an arbitrary wave generator (AWG; Keysight 33210A). The Joule heating, $Q(t)$, generated by the electrical modulation, changes the device temperature $T(t)$ over time, and the device then radiates the thermal infrared emission, $I(\lambda, T(t))$ (optical signal). An infinite-corrected reflective objective collects the modulated $I(\lambda, T(t))$ and directs it to the FTIR (Thermo Fisher iS50) for interferometry using a dichroic beam splitter through an aperture. Here, the aperture can block the noises from structures surrounding the DUT and provide

the space-resolved capability when the DUT emission is inhomogeneous. The beam splitter transmits white light (from an external illumination) reflected by DUT to locate and focus on the active area of DUT using a microscope subsystem under a CCD camera. The step-scan mode is used to avoid the double modulation issue arising when coupling the FTIR and the LIA [41]. The interferogram $S_{\text{in}}(\lambda, t)$ recorded by a mercury-cadmium-telluride (MCT) detector is fed to the LIA (Zurich Instruments HF2LI), which works as a dynamic noise filter centered at the reference frequency that can be the modulation frequency or its higher-order harmonics. The MCT detector that has an original specific detectivity of 8.0×10^9 Jones can be further boosted by the LIA with a dynamic reserve of 120 dB, leading to a total specific detectivity of 8.0×10^{15} Jones for our lock-in FTIR system. This ultrahigh specific detectivity allows us to overcome the heavy optical loss and background noise during the emission light collection. Finally, the output voltage $S_{\text{out}}(\lambda)$ from the LIA represents the emission intensity of the DUT.

To illustrate the signal-detection process, we define the mathematical relations between the parameters in each processing step. The translation of the signal from the modulation voltage $V(t)$ to the thermal emission $I(\lambda, T(t))$ depends on a thermos-opto-electrical design of the DUT. In this work, we use an electrically driven thermal infrared metasurface with an active area (red-dashed box) of about $50 \times 50 \mu\text{m}^2$, as shown in Fig. 1(b). The metasurface is composed of a gold nanorod array and adopts a center-contacted electrode line design, which not only enables a narrowband emissivity resonance at around $5.24 \mu\text{m}$, but also allows a fast Joule heating to modulate the thermal emission [42]. To obtain the temperature $T(t)$ of the metasurface under a given voltage $V(t)$, we neglect the top-surface radiation and natural convection since heat dissipation into the substrate dominates. As we collect only the emission from the active metasurface area (confined by the aperture) that is approximately isothermal, as verified by thermal infrared mapping [42], we can model the electrothermal design of the DUT as one-dimensional heat conduction to the substrate. To include the transient thermal response, we further simplify the heat transfer as an equivalent thermal circuit using the lumped capacitance model, as shown in Fig. 1(c). Based on this model, we separate the substrate into two control volumes, represented by two nodes $T(t)$ and T_0 , via the dashed line that is roughly defined by the thermal penetration depth. The control volume with $T(t)$ can store energy with a thermal capacitance C_t , or transfer heat to the control volume with T_0 (grounded) below via a thermal resistance R_t . The metasurface serves as a heat source $Q(t)$. Via the lumped capacitance model, we have the dynamic equation

$$C_t \frac{d(T(t) - T_0)}{dt} + \frac{T(t) - T_0}{R_t} = Q(t), \quad (1)$$

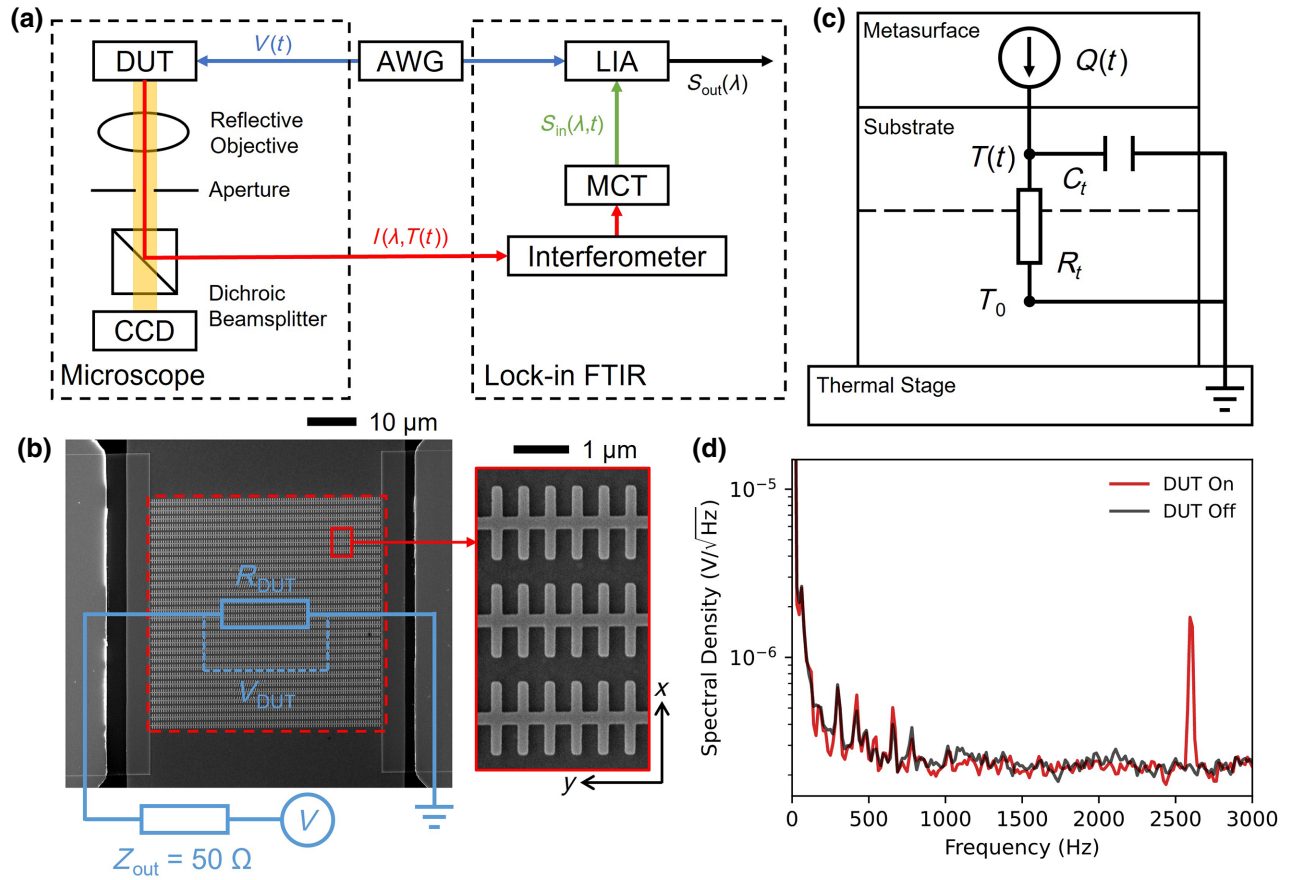


FIG. 1. Measurement setup and device design. (a) Schematic of the microscopic lock-in FTIR system setup and its signal-detection process. (b) Top view SEM images of the electrothermal metasurface with a gold nanorod array for narrowband emission. The emission active area (red-dashed box) is about $50 \times 50 \mu\text{m}^2$. The inset shows the dimensions of the metasurface: periodicities $P_x = 1.8 \mu\text{m}$, $P_y = 0.5 \mu\text{m}$, length $L = 1.3 \mu\text{m}$, and width $W = 0.15 \mu\text{m}$. The schematic of an equivalent electrical circuit model demonstrates the power injection for Joule heating. (c) Schematic of an equivalent thermal circuit model for the electrothermal response of the metasurface. (d) Input voltage spectral densities of DUT on (S_{in} modulated at 2600 Hz) and DUT off.

where $Q(t) = V_{\text{DUT}}^2(t)/R_{\text{DUT}}$ is the Joule heating and R_{DUT} is the electrical resistance of the metasurface. Based on the equivalent electrical circuit model for Joule heating shown in Fig. 1(b), we can define an effective electrical resistance $R = (Z_{\text{out}} + R_{\text{DUT}})^2/R_{\text{DUT}}$ with $Q(t) = V^2(t)/R$. This linear first-order ordinary differential equation can be solved by constructing an exact differential with an integrating factor $\mu(t) = (1/C_t)e^{t/R_t C_t}$. The solution $T(t)$, with the initial condition $T(0) = T_0$, is given by

$$T(t) = T_0 + T_0 e^{-t/(R_t C_t)} + \frac{e^{-t/(R_t C_t)}}{C_t} \int_0^t e^{t'/R_t C_t} Q(t') dt'. \quad (2)$$

With the derived temperature $T(t)$ of the emitting region, thermalization of which happens much faster than the temperature modulation speed, we can then compute the spectral thermal emission based on Planck's law in a time-pointwise manner as $I(\lambda, t) = \epsilon(\lambda) I_{\text{BB}}(\lambda, T(t))$ where $I_{\text{BB}}(\lambda, T(t))$ is the blackbody emission spectrum at temperature $T(t)$ and $\epsilon(\lambda)$ is the emissivity of the metasurface.

The Joule heating generated by $V(t)$ has two parts: one is the time-independent part due to the root-mean-square of the power, and the other is the time-dependent part arising from modulation. Consequently, $T(t)$ can be expressed as $T(t) = T_0 + T_{\text{dc}} + T_m(t) = T_{\text{avg}} + T_m(t)$ where T_{dc} and $T_m(t)$ are the time-independent and time-dependent parts of temperature, respectively. We can further group T_0 and T_{dc} as the average temperature T_{avg} of the emitting region, which can be measured from a thermal mapping system [42]. Since $T_m(t) \ll T_{\text{avg}}$, $I_{\text{BB}}(\lambda, T(t))$ can be expanded using the Taylor expansion with respect to $T(t)$ as

$$I(\lambda, t) = \epsilon(\lambda) I_{\text{BB}}(\lambda, T_{\text{avg}}) + \epsilon(\lambda) \frac{\partial I_{\text{BB}}}{\partial T}(\lambda, T_{\text{avg}}) T_m(t), \quad (3)$$

which defines the thermal emission from the DUT (optical signal collected by the reflective objective). The optical signal reaching the MCT detector is then transformed to a

voltage input $S_{\text{in}}(\lambda, t)$ to the LIA as

$$S_{\text{in}}(\lambda, t) = r(\lambda)I(\lambda, T) + S_{\text{noise}} = r(\lambda) \left(\varepsilon(\lambda)I_{\text{BB}}(\lambda, T_{\text{avg}}) + \varepsilon(\lambda) \frac{\partial I_{\text{BB}}}{\partial T}(\lambda, T_{\text{avg}})T_m(t) \right) + S_{\text{noise}}, \quad (4)$$

where $r(\lambda)$ is the response function whose wavelength dependence comes from MCT responsivity and other optical components along the optical path. S_{noise} is the total unmodulated noise that can be filtered out by the LIA. As shown in Fig. 1(d), when switching (modulating) the input signal to a modulation frequency of 2600 Hz, we find that the noises at 2600 Hz (DUT off) are small as compared to the signal value (DUT on). This means that by removing the unmodulated noises at 0 Hz, we can already obtain a good SNR for the demodulated output.

III. JOULE AND GLOBAL HEATING FOR NOISE REDUCTION

Starting with the voltage input $S_{\text{in}}(\lambda, t)$ to the LIA in Eq. (4), we can explore the effects of the Joule heating and global heating on the SNR. Specifically, we first demonstrate that the dc bias and ac wave shapes of the Joule heating play a central role in optimizing the LIA for noise reduction. The reference temperature T_0 given by the global heating, though unmodulated, is also found to significantly enhance the final output signal from the LIA.

To figure out the influence of the dc bias on the final detected signal, we start with a simple modulation voltage as

$$V(t) = V_p \cos(2\pi ft) + V_0, \quad (5)$$

which is a cosine signal with a peak voltage V_p and a dc bias V_0 . The Joule heating can be expressed as $Q(t) = V^2(t)/R = Q_{\text{dc}} + Q_{1f}(t) + Q_{2f}(t)$ where the dc Joule heating is $Q_{\text{dc}} = V_p^2/2R + V_0^2/R$ and the first and second harmonics of the Joule heating are $Q_{1f}(t) = (2V_p V_0/R)(e^{i\omega t} + e^{-i\omega t})/2$ and $Q_{2f}(t) = (V_p^2/2R)(e^{i2\omega t} + e^{-i2\omega t})/2$, respectively. Here, we use complex representations for convenience and keep the complex conjugate terms to fully express the real physical quantity since the measurement system is not all linear. The steady-state temperature of DUT is then given by inserting the dc and harmonic Joule heating terms into Eq. (2), and since $T(t)$ is linearly dependent on $Q(t)$, we find that $T(t)$ can also be

expressed in terms of its harmonics as

$$\begin{aligned} T(t) &= T_{1f}(t) + T_{2f}(t) + T_{\text{dc}} \\ &= \frac{2V_p V_0 R_t}{R} \frac{1}{1 + \omega^2 R_t^2 C_t^2} (\cos \omega t + \omega R_t C_t \sin \omega t) \\ &\quad + \frac{V_p^2 R_t}{2R} \frac{1}{1 + 4\omega^2 R_t^2 C_t^2} (\cos 2\omega t + 2\omega R_t C_t \sin 2\omega t) \\ &\quad + \left(\frac{V_p^2}{2R} + \frac{V_0^2}{R} \right) R_t + T_0. \end{aligned} \quad (6)$$

Under global heating of $T_0 = 125$ °C, the electrical resistance is measured as $R_{\text{DUT}} = 8.9$ Ω. The thermal resistance due to heat conduction can be estimated as $R_t = 974.5$ K/W by a dc voltage $V(t) = V_{\text{dc}} = 2.0$ V with $R_t = (T_{\text{dc}} - T_0)/Q_{\text{dc}}$ where $T_{\text{dc}} = 135$ °C is obtained from the thermal mapping and $Q_{\text{dc}} = V_{\text{dc}}^2/R$, still under global heating of $T_0 = 125$ °C. Here, we ignore the heat loss from convection and radiation. The thermal time constant $R_t C_t = 1.6$ μs can be obtained from the discussion in Sec. IV, again under global heating of $T_0 = 125$ °C. With an input of $V_p = 1.0$ V, $f = 2600$ Hz, and $T_0 = 125$ °C, we can demonstrate the input voltages $V(t)$ and their temperature swing on the metasurface for $V_0 = 0.0$ V, 0.5 V, 1.0 V in Fig. 2(a). Clearly, the nonzero dc bias V_0 generates a $1f$ temperature swing for the metasurface thermal emission.

After substituting $T(t)$ into Eq. (4), we obtain the LIA input $S_{\text{in}}(\lambda, t)$. Based on the working principle of LIA, $S_{\text{in}}(\lambda, t)$ is then mixed with a reference $S_{\text{ref}}(t) = e^{-i(2\pi f_r t + \Delta\phi)}$ for a dual-phase demodulation, and the fixed phase difference $\Delta\phi$ between $S_{\text{in}}(\lambda, t)$ and $S_{\text{ref}}(t)$ can be finally canceled [43]. The final output from the mixed signal $S_{\text{mix}}(\lambda, t) = S_{\text{in}}(\lambda, t) \cdot S_{\text{ref}}(t)$ depends on the order of its harmonics that we choose via the reference frequency f_r . If we select $f_r = 1f$ (first harmonic), the magnitude of the dc output after the low-pass filter in the LIA is

$$\begin{aligned} S_{\text{out},1f}^{\text{cos}}(\lambda) &= r(\lambda)\varepsilon(\lambda) \frac{\partial I_{\text{BB}}}{\partial T}(\lambda, T_{\text{avg}}) \frac{V_p V_0 R_t}{R} \\ &\quad \times \frac{1}{\sqrt{1 + (2\pi f)^2 R_t^2 C_t^2}} \end{aligned} \quad (7)$$

and if selecting $f_r = 2f$ (second harmonic), we have the output signal

$$\begin{aligned} S_{\text{out},2f}^{\text{cos}}(\lambda) &= r(\lambda)\varepsilon(\lambda) \frac{\partial I_{\text{BB}}}{\partial T}(\lambda, T_{\text{avg}}) \frac{V_p^2 R_t}{4R} \\ &\quad \times \frac{1}{\sqrt{1 + 4(2\pi f)^2 R_t^2 C_t^2}}. \end{aligned} \quad (8)$$

We also observe that the unmodulated portion of thermal emission together with the noises are always at $f_r \neq 0$, and finally filtered out.

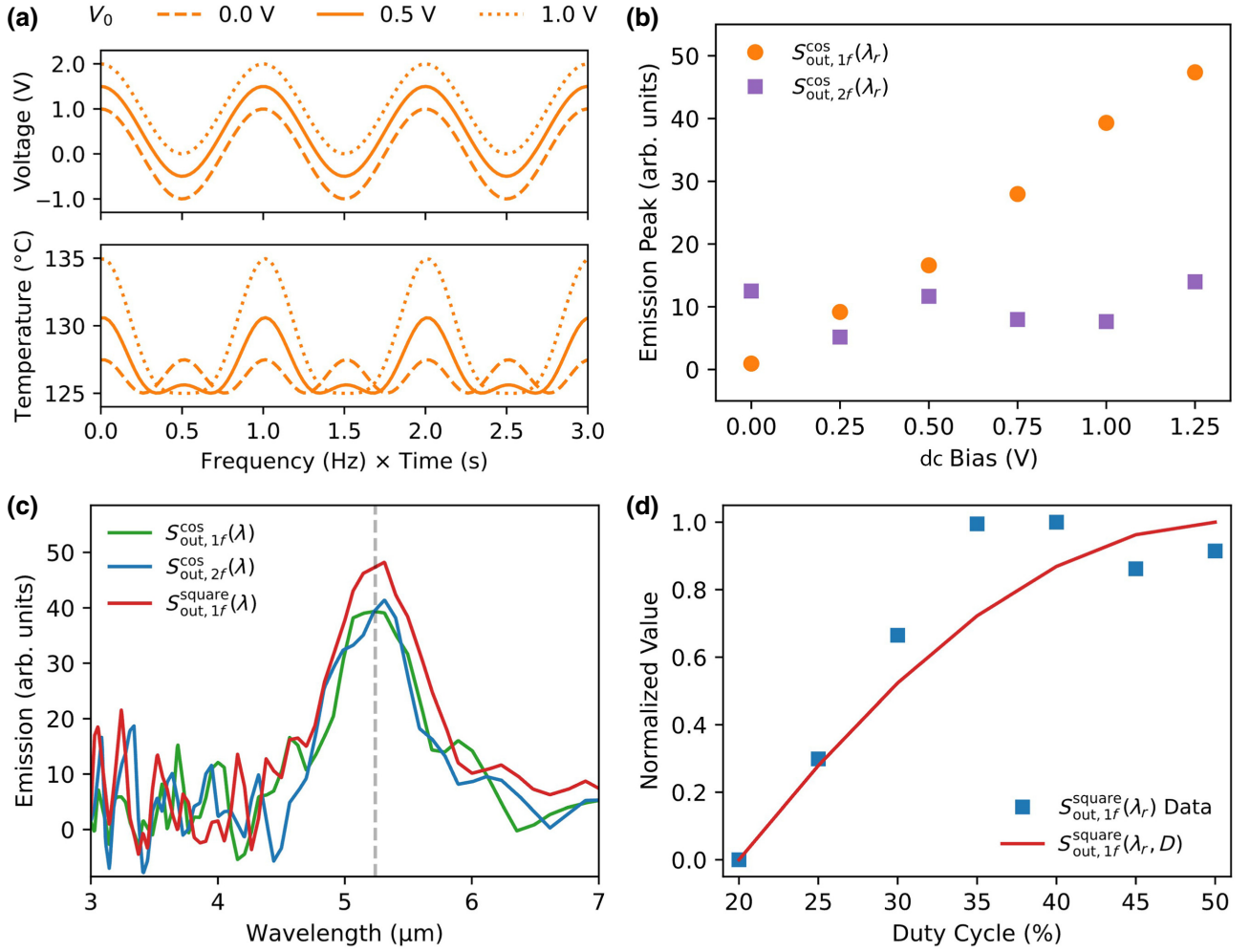


FIG. 2. Analysis of the effect of Joule heating on thermal emission. (a) Input voltages $V(t)$ with $V_0 = 0.0$ V, 0.5 V, 1.0 V and their temperature swings on the metasurface for a biased cosine wave with $V_p = 1.0$ V, $f = 2600$ Hz, and $T_0 = 125$ °C. (b) Emission peaks $S_{\text{out},1f}^{\text{cos}}(\lambda_r)$ and $S_{\text{out},2f}^{\text{cos}}(\lambda_r)$ at $\lambda_r = 5.24 \mu\text{m}$ from the LIA under different dc biases V_0 , under $V_p = 1.0$ V, $T_0 = 125$ °C, and $f = 2600$ Hz. (c) Emission spectra of $S_{\text{out},1f}^{\text{cos}}(\lambda)$ with ($V_0 = V_p = 1.0$ V) and $S_{\text{out},2f}^{\text{cos}}(\lambda)$ with ($V_p = 2.0$ V, $V_0 = 0.0$ V), under $T_0 = 125$ °C and $f = 2600$ Hz. The wave shape can further boost the SNR, as indicated by the $4/\pi$ factor increment at resonance λ_r (gray-dashed line) of $S_{\text{out},1f}^{\text{square}}(\lambda)$ by a square pulse train modulation ($V_s = 2.0$ V, $D = 50\%$) compared to $S_{\text{out},1f}^{\text{cos}}(\lambda)$. (d) Normalized emission peak data $S_{\text{out},1f}^{\text{square}}(\lambda_r)$, as a function of duty cycle D of the square pulse train, under $V_s = 3.0$ V, $T_0 = 125$ °C, and $f = 2600$ Hz, keeps consistent with the analytical formula $S_{\text{out},1f}^{\text{square}}(\lambda_r, D)$.

Therefore, it is worthwhile to note that we can use the first harmonic of the Joule heating for signal detection due to the electrical modulation as a combination of ac cosine wave and dc bias, unlike the previous studies [30], which always focus on the full-wave rectified cosine wave with $2f$ for the reference frequency. Of note, the filtered output signal $S_{\text{out},1f}^{\text{cos}}(\lambda)$ is proportional to the dc bias V_0 such that we can overcome the power limit of the AWG by connecting a dc source in series to increase the signal input. To examine the dependence of the first and second harmonics of the output signal on V_0 , we vary V_0 and keep constant $V_p = 1.0$ V and measure the emission peak $S_{\text{out},1f}^{\text{cos}}(\lambda_r)$ at $\lambda_r = 5.24 \mu\text{m}$ [at gray dashed line shown in Fig. 2(c)] under $T_0 = 125$ °C and $f = 2600$ Hz.

For this measurement, we approximate $T_{\text{avg}} = T_{\text{dc}} + T_0 \approx T_0$ because T_{dc} generated from the low modulation voltages is much smaller than T_0 , and $2\pi f R_l C_l \approx 0$ because $T_0 \gg T_{\text{dc}}$ and $f \ll f_{3\text{dB}} = 1/2\pi R_l C_l$ where $f_{3\text{dB}}$ is the DUT cutoff frequency and can be verified in our frequency response analysis later. As shown in Fig. 2(b), the emission peak $S_{\text{out},1f}^{\text{cos}}(\lambda_r)$ increases linearly with increasing V_0 while $S_{\text{out},2f}^{\text{cos}}(\lambda_r)$ keeps approximately constant with fixed V_p . The crossing point of equal emission peak with about $V_p = 1.0$ V and $V_0 = 0.25$ V can be well verified by theoretical predictions calculated using Eq. (7) for $S_{\text{out},1f}^{\text{cos}}(\lambda_r)$ and Eq. (8) for $S_{\text{out},2f}^{\text{cos}}(\lambda_r)$. These two formulas can also be verified by full spectra of the signals with two input voltage sets: ($V_p = V_0 = 1.0$ V) for $S_{\text{out},1f}^{\text{cos}}(\lambda)$ and

($V_p = 2.0$ V, $V_0 = 0.0$ V) for $S_{\text{out},2f}^{\text{cos}}(\lambda)$ in the LIA. Based on Eqs. (7) and (8), they should have the same emission spectra, which are experimentally verified in Fig. 2(c). Counterintuitively, the dc Joule heating contributes to the modulated signal based on its nonlinear electrical interference with the ac Joule heating as estimated in $Q_{1f}(t)$, which makes it fundamentally different from the global heating.

The output signal can also benefit from the wave shape of the modulation. If we change the cosine pulse train to a square pulse train, the modulation voltage can be defined as

$$V(t) = V_s D + \sum_{n=1}^{N=\infty} \frac{2V_s}{n\pi} \sin(nD\pi) \cos(n2\pi ft), \quad (9)$$

where D is the duty cycle, V_s is the pulse height, and N denotes the number of harmonics. Following the same process as the above, we obtain the DUT temperature as $T(t) = T_0 + T_{\text{dc}} + T_{1f}(t) + \dots$ and the magnitude of the $f_r = 1f$ (first harmonic) output voltage as

$$\begin{aligned} S_{\text{out},1f}^{\text{square}}(\lambda) &= r(\lambda)\varepsilon(\lambda) \frac{\partial I_{\text{BB}}}{\partial T}(\lambda, T_{\text{avg}}) \frac{R_t}{2R} \\ &\times \left\{ \frac{4V_s^2 D}{\pi} \sin(D\pi) + \frac{V_s^2}{\pi^2} \sin(D\pi) \sin(2D\pi) \right. \\ &+ \frac{2V_s^2}{\pi^2} \sum_{n=2}^{N=\infty} \left[\frac{1}{n(n-1)} \sin(nD\pi) \sin((n-1)D\pi) \right. \\ &+ \left. \left. \frac{1}{n(n+1)} \sin(nD\pi) \sin((n+1)D\pi) \right] \right\} \\ &\times \frac{1}{\sqrt{1 + (2\pi f)^2 R_t^2 C_t^2}}. \end{aligned} \quad (10)$$

We compare the square pulse train ($V_s = 2.0$ V, $D = 50\%$) and the cosine pulse train ($V_p = V_0 = 1.0$ V) under $T_0 = 125^\circ\text{C}$ and $f = 2600$ Hz, where V_s , D , V_0 , and V_p are set to have the same period and pulse height for both pulse trains except for the wave shape. T_0 and f are set to maintain the approximations of $T_{\text{avg}} \approx T_0$ and $2\pi f R_t C_t \approx 0$, respectively. A $4/\pi$ factor increment in the output signal is expected and observed in Fig. 2(c) with the emission peak ratio $S_{\text{out},1f}^{\text{square}}(\lambda_r)/S_{\text{out},1f}^{\text{cos}}(\lambda_r)$ at emission resonance $\lambda_r = 5.24 \mu\text{m}$ (at gray dashed line) about 1.2. In addition, $S_{\text{out},1f}^{\text{square}}(\lambda)$ is also a function of D . To demonstrate this, in Fig. 2(d), we change D and measure the emission peak $S_{\text{out},1f}^{\text{square}}(\lambda_r)$ with $V_s = 3.0$ V, $T_0 = 125^\circ\text{C}$, and $f = 2600$ Hz, whose data is well consistent with the analytical expression $S_{\text{out},1f}^{\text{square}}(\lambda_r, D)$ from Eq. (10). Here, we perform a minimum-maximum normalization for both $S_{\text{out},1f}^{\text{square}}(\lambda_r)$ and $S_{\text{out},1f}^{\text{square}}(\lambda_r, D)$ to scale their values in the range of (0, 1), and use $N = 38$ in our computation because the number of harmonic terms required to approximate a square pulse

wave shape depends on the DUT response speed. More specifically, $Nf \leq f_{3\text{dB}}$ where $f_{3\text{dB}} = 100$ kHz is the cut-off frequency of our metasurface (discussed below). More advanced wave shapes of the modulation can be applied to further benefit the emission measurement, all of which can be accurately explored based on our signal process analysis.

After deriving the formulas for the LIA output [Eqs. (7), (8), and (10)], we are now able to demonstrate the effect of global heating on the SNR. We choose a square pulse train with $V_s = 3.0$ V, $D = 50\%$, and $f = 2600$ Hz as the modulation voltage $V(t)$ and measure the emission spectra $S_{\text{out},1f}^{\text{square}}(\lambda)$ under different global heating temperatures T_0 . As shown in Fig. 3(a), with T_0 increasing from 25°C to 150°C , the intensity of $S_{\text{out},1f}^{\text{square}}(\lambda)$ enhances significantly because T_0 greatly increases the blackbody emission as indicated by the term $\partial I_{\text{BB}}(\lambda, T_{\text{avg}})/\partial T$ in Eq. (10), although T_0 itself is unmodulated. This increasing effect is strong and overwhelms the decreasing effect [$S_{\text{out},1f}^{\text{square}}(\lambda) \propto 1/R$ from Eq. (10)] from the effective electrical resistance R that is increased by the global heating temperature $T_0 \approx T_{\text{avg}}$. Since the influence from blackbody emission $\partial I_{\text{BB}}(\lambda, T_{\text{avg}})/\partial T$ is the same for all the harmonics of $S_{\text{out},1f}^{\text{square}}(\lambda)$, the emission enhancement from T_0 works for any wave shape based on Joule heating, including the simple cosine wave shape as indicated by Eqs. (7) and (8). To specify the SNR increment from T_0 , we repeatedly measure the emission spectra of $T_0 = 25^\circ\text{C}$ and 125°C for 5 times and calculate the SNR based on [44]

$$\text{SNR}(\lambda) = \frac{\bar{S}_{\text{out},1f}^{\text{square}}(\lambda) - S_{\text{out},1f}^{\text{off}}(\lambda)}{\sigma_{\text{out},1f}^{\text{square}}(\lambda)}, \quad (11)$$

where $\bar{S}_{\text{out},1f}^{\text{square}}(\lambda)$ and $\sigma_{\text{out},1f}^{\text{square}}(\lambda)$ are the mean and standard deviation of repeatedly measured emission spectra, respectively. $S_{\text{out},1f}^{\text{off}}(\lambda)$ is the emission spectrum when the DUT is off, i.e., without the Joule heating. As shown in Fig. 3(b), even under the room temperature (25°C), the $\text{SNR}(\lambda)$ can go beyond the true-signal-threshold [40] ($\text{SNR} = 3.0$; red-dashed line) near the resonance region with $\text{SNR}(\lambda_r) = 7.9$. The region that is above the true-signal-threshold then extends notably when we increase T_0 to 125°C , and $\text{SNR}(\lambda_r)$ reaches 23.7. Thanks to the strong noise reduction from our lock-in FTIR system, we require only a much smaller T_0 ($25 - 125^\circ\text{C}$), compared to the previous direct measurements of far-field emission that is generated by a temperature more than 480°C [23,24]. The heating temperature required by our system is only about 1/3 or even 1/20 of that needed in the previous studies, and this temperature can be further reduced if we keep optimizing the parameter setup in the LIA. Although the device with a higher temperature is also easier to obtain a high-SNR spectrum based on our system, the possible errors may come from the stability of the device that needs a

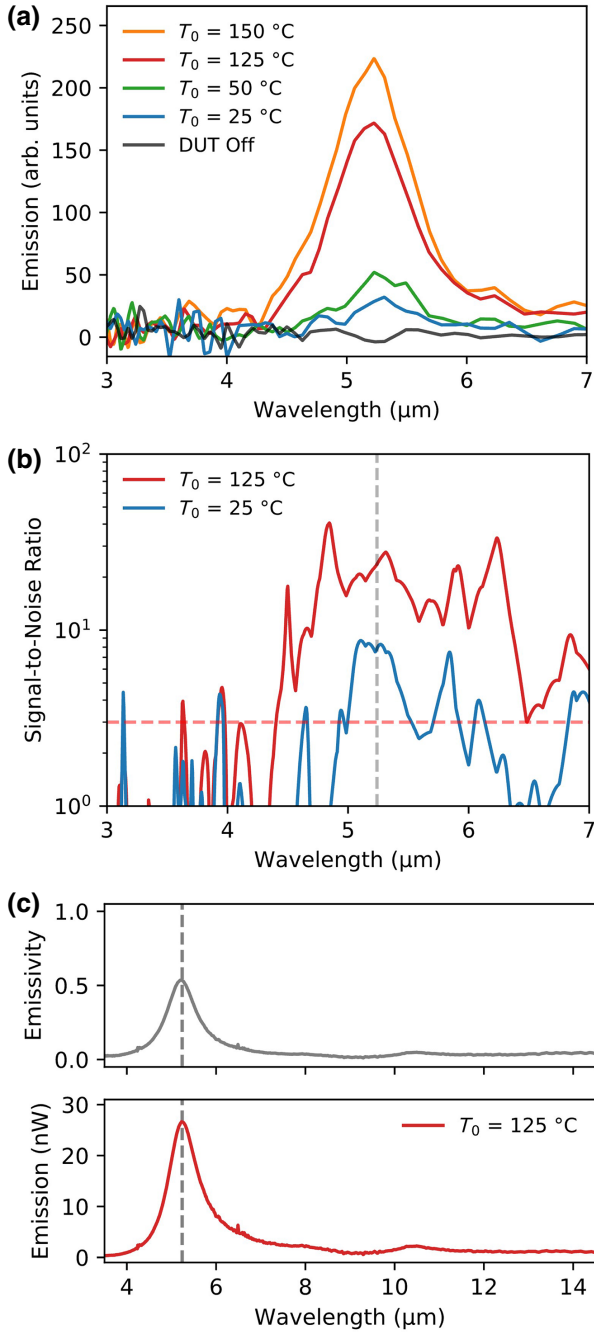


FIG. 3. Analysis of the effect of global heating on thermal emission. (a) The emission spectra $S_{\text{out},lf}^{\text{square}}(\lambda)$ under different T_0 , under $V_s = 3.0$ V, $D = 50\%$, and $f = 2600$ Hz. Although unmodulated, T_0 increases the blackbody emission resulting in the magnitude increment for $S_{\text{out},lf}^{\text{square}}(\lambda)$. (b) The SNR for $T_0 = 25$ °C and 125 °C with five repeated measurements. With T_0 increasing from 25 to 125 °C, the region above the true-signal-threshold (SNR about 3.0; red-dashed line) enlarges the SNR at the resonance $\lambda_r = 5.24$ μm (gray-dashed line) increases from 7.9 to 23.7. (c) The emissivity of metasurface from the FTIR reflectance measurement, and the spectral emission power of metasurface with a square pulse train $V_s = 3.0$ V, $D = 50\%$, and $f = 2600$ Hz, under global heating of 125 °C.

high-power input to maintain the high temperature because the data-collection time of our system is typically longer than the conventional rapid-scan mode of FTIR. Also, when the temperature is extremely high, the air surrounding the sample may change the refraction index, resulting in some loss in the light collection of the microscopic objective. A high-magnification objective, typically with a short working distance, may get damaged because it gets so close to the extremely hot sample. We also notice that the SNR drops at the wavelengths around 3 – 4 μm and 6 – 7 μm due to the optical loss from H₂O and CO₂ absorption, respectively, which can be solved by purging our optical paths with N₂ gas.

Besides SNR, another aspect of the emission measurement is the spectral resolution, which theoretically depends on the traveling range of the moving mirror inside the FTIR equipment. An infinitely high resolution can be obtained if one can scan the moving mirror for an infinitely long distance. In practice, a limited traveling distance of the moving mirror causes a finite resolution and ripples (Gibbs' phenomenon) for the spectrum. The ripples are a source of noises that deforms the spectrum and are alleviated by an apodization function, which however can cause the degradation of resolution [45]. In our system, we balance this trade-off with the Happ-Genzel apodization function. A boxcar apodization function can be used when a higher resolution is required, although the ripples may not be well suppressed. In addition, increasing the resolution typically reduces the SNR and significantly increases the data collection time [46]. This is another factor for consideration, if a higher resolution of our system is needed.

Finally, to gauge the ultrahigh sensitivity of our measurement system, we estimate the emission power from the metasurface to the measurement system via Planck's law in nW as $I_{\text{BB}}(\lambda, T) = (c_1 A \Omega \times 10^9) / [\lambda^5 (e^{c_2/\lambda T} - 1)]$ with $c_1 = 1.191042 \times 10^8$ W/m² sr um⁻⁴ and $c_2 = 1.438775 \times 10^4$ K/ μm , after including the size $A = 50 \times 50$ μm^2 of metasurface [red-dashed area in Fig. 1(b)], the solid angle $\Omega = 0.53$ of the microscope (Thorlabs reflective objective LMM40X-P01), and the temperature $T = 137$ °C of metasurface from the thermal mapping under a square pulse train $V_s = 3.0$ V, $D = 50\%$, and $f = 2600$ Hz, under the global heating of 125 °C. We then measure the emissivity spectrum $\varepsilon(\lambda)$ from the FTIR reflectance measurement based on Kirchhoff's law. The spectral emission power of the metasurface can thus be calculated as $I_{\text{DUT}}(\lambda) = \varepsilon(\lambda) I_{\text{BB}}(\lambda, T)$ and shown in Fig. 3(c). The total emission power is estimated as the integral over the entire spectrum as $I_{\text{DUT}} = 8.3$ μW .

IV. SPECTRAL-RESOLVED FREQUENCY RESPONSE

After obtaining the emission spectra with a high SNR, we can further characterize the frequency response of the

DUT. Under $T_0 = 125^\circ\text{C}$, we choose the square pulse train with $V_s = 3.0\text{ V}$ and $D = 50\%$ to take advantage of the $4/\pi$ increment factor as compared to a conventional cosine pulse train. At the same time, the 50% duty cycle enables elimination of the summation of N harmonic terms from the wave-shape deformation that can complicate the frequency response measurement, as discussed in Fig. 2. The measured output voltage is then obtained from Eq. (10) as

$$S_{\text{out},1f}^{\text{square}}(\lambda, f) = r(\lambda)\varepsilon(\lambda) \frac{\partial I_{\text{BB}}}{\partial T}(\lambda, T_{\text{avg}}) \frac{V_s^2 R_t}{\pi R} \frac{1}{\sqrt{1 + (2\pi f)^2 R_t^2 C_t^2}}. \quad (12)$$

We record the entire emission spectrum at each modulation frequency f and characterize the dynamic response with f up to one with a low emission intensity, as shown in Fig. 4(a). It is worthwhile to note that we can obtain the full spectrum of the emission as our dynamic response characterization is spectrally resolved. This can be particularly useful for the modulation mechanisms other than the emission power. To characterize the response speed, we plot the emission peak (gray-dashed line) $S_{\text{out},1f}^{\text{square}}(\lambda_r, f)$ as the function of the modulation frequency f in Fig. 4(b), together with the temperature response $T_{m,1f}(f)$ of the metasurface via a thermal simulation using COMSOL Multiphysics. Three COMSOL modules, including electrical circuits, electrical current, and heat transfer in solids, are adopted to describe the Joule heating process on the device. The electrical circuits' module models the cosine voltage source with $50\ \Omega$ internal resistance. The voltage source has an offset voltage of 2.1 V and the amplitude of 0.5 V , and the frequency of the voltage source is swept from 1.5 to 200 kHz . The output of this voltage source is then transferred to electrical current module, where the voltage Poisson equation is solved for the metasurface region, and the Joule-heat generation is calculated based on current density and resistivity of the material. Finally, the heat-transfer module solves the heat-transfer equation to obtain the device temperature. The bottom surface of the Si substrate is set to 125°C , corresponding to the global heating temperature. The Joule-heat generation from the electrical current module acts as a volumetric heat source on the metasurface. The volumetric average temperature of the metasurface then changes with the same frequency ($1f$) as the input biased cosine voltage [as discussed in Fig. 2(a)], and to indicate the thermal response we select the peak temperature of the temperature swing $T_{m,1f}$, which is $T(t) - T_0 - T_{\text{dc}} = T(t) - T_{\text{avg}}$ as discussed in Sec. II. The device structure is restructured from Ref. [42], and the thermal properties of the incorporated materials, consisting of Si, SiO_2 , Al_2O_3 , and Au, are from Refs. [47–50]. The

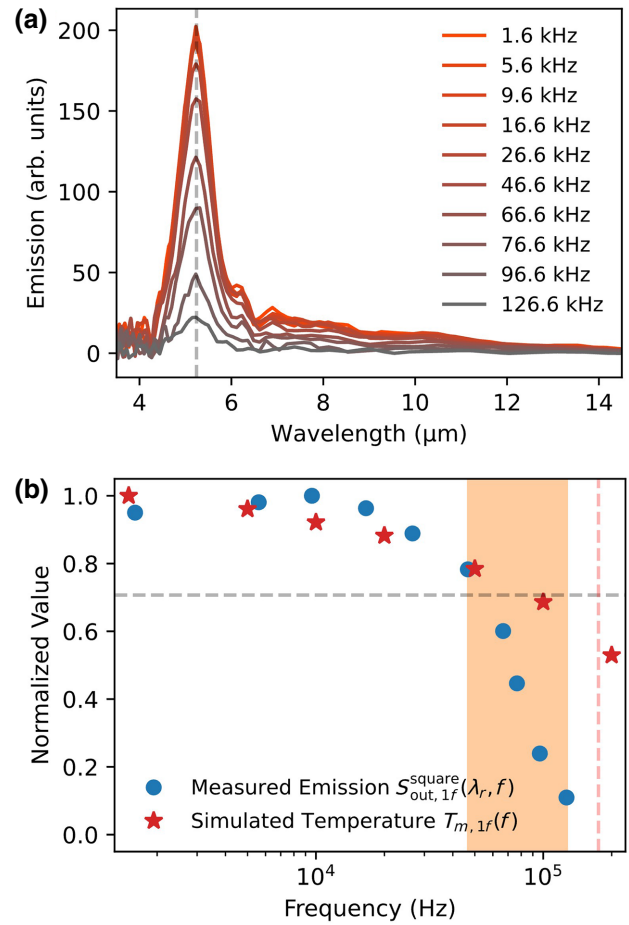


FIG. 4. Spectral-resolved frequency-domain dynamic characterization. (a) Emission spectrum $S_{\text{out},1f}^{\text{square}}(\lambda)$ at each modulation frequency f , under a square pulse train modulation $V(t)$ ($V_s = 3.0\text{ V}$, $D = 50\%$) and $T_0 = 125^\circ\text{C}$. (b) Emission peaks $S_{\text{out},1f}^{\text{square}}(\lambda_r, f)$ at $\lambda_r = 5.24\ \mu\text{m}$ and simulated temperatures $T_{m,1f}(f)$ under different modulation frequencies f .

electrical conductivity of Au is selected as $2.36 \times 10^7\text{ S/m}$ based on a measured device resistance of $8.9\ \Omega$.

Based on our analytical signal model of Eqs. (3) and (4), for the source voltage $V(t)$ with either a biased cosine wave or a square pulse train with 50% duty cycle, their respective $1f$ outputs in Eqs. (7) and (12) should be proportional to the temperature swing $T_{m,1f}(f)$. The constant proportional ratio can be canceled out with a maximum normalization, and we can directly compare the measured emission response and the simulated temperature response as shown in Fig. 4(b). For frequencies of 1.5 and 5 kHz , the respective $T_{m,1f}(f)$ is 5.1 and 4.9°C , and we believe that the metasurface device at this frequency range can instantaneously follow the input modulation, compared to the $T_{m,1f}(f)$ of 2.7°C for 200 kHz . Therefore, the maximum normalization should be valid for both measured emissions and simulated temperatures.

For frequencies lower than 47 kHz, the measured emission $S_{\text{out},1f}^{\text{square}}(\lambda_r, f)$ is consistent with the simulated temperature $T_{m,1f}(f)$, but there is an increasing dropping of $S_{\text{out},1f}^{\text{square}}(\lambda_r, f)$ compared to $T_{m,1f}(f)$ for higher frequencies (orange area), indicating the proportional ratio of emission to temperature is nonconstant in this frequency range. The cutoff frequencies (3 dB labeled as the gray-dashed line) of $S_{\text{out},1f}^{\text{square}}(\lambda_r, f)$ and $T_{m,1f}(f)$ then bear a large difference, with the former one of 50 kHz and the latter one of 100 kHz. To explain the deviation of the measured emission response and simulated temperature response, we focus on Eq. (12) of $S_{\text{out},1f}^{\text{square}}(\lambda_r, f)$. The average temperature T_{avg} changes only slightly for different modulation frequencies from our thermal simulation (the global heating T_0 is dominant for T_{avg}), indicating that the $\partial I_{\text{BB}}(\lambda, T_{\text{avg}})/\partial T$ and R also approximately keep constant for different frequencies. Thus, the nonconstant proportional ratio of emission to temperature comes from the system response function $r(\lambda_r, f)$, that is, the cutoff frequency of our system is smaller than 175 kHz (red-dashed line), which is given by the preamplifier connecting to the MCT detector. The dropping of the measured emission is then the accumulated effect from both the frequency-dependent system response function and the device response. Although our proposed spectral-resolved dynamic measurement for thermal emission is still feasible, we should admit that the trustworthy measurable frequency range of our system is limited to 47 kHz. However, because the measured emission at 127 kHz still has a decent SNR, as shown in Fig. 4(a), it is possible to extend the measurable frequency range of our system up to this frequency with calibrations of the system response function $r(\lambda, f)$ for the higher frequencies (orange area). We thus can summarize the measurable frequency range of our lock-in FTIR system for spectral-resolved thermal emission dynamics: 47 kHz without calibration and 127 kHz with calibration.

To calibrate the system response function $r(\lambda, f)$, we can use a known modifiable infrared source (either a blackbody source or an infrared LED) and measure its emission spectra by changing the modulation frequency f . The calibrated $r(\lambda, f)$ can not only extend the measurable frequency range for the spectral-resolved frequency response measurement, but also recover the emissivity from the emission with the definition of spectral emissivity $\varepsilon(\lambda) = I(\lambda, T_{\text{avg}})/I_{\text{BB}}(\lambda, T_{\text{avg}})$. The (optical) emission intensity can then be recovered by $I(\lambda, T_{\text{avg}}) = S(\lambda, T_{\text{avg}})/r(\lambda)$. With the temperature T_{avg} , we can also compute the blackbody emission intensity $I_{\text{BB}}(\lambda, T_{\text{avg}})$ based on Planck's law. Therefore, the spectral emissivity becomes $\varepsilon(\lambda) = S(\lambda, T_{\text{avg}})/[r(\lambda)I_{\text{BB}}(\lambda, T_{\text{avg}})]$. Another method for emissivity calibration is to directly use the (electrical) emission signal $S(\lambda, T_{\text{avg}})$, which is the product of $r(\lambda)I(\lambda, T_{\text{avg}})$. We can then measure the emission signal from a blackbody source, $S_{\text{BB}}(\lambda, T_{\text{avg}})$ with the same temperature T_{avg} , under

the exact same measurement conditions including both optical and electrical setups. Thus, the spectral emissivity becomes $\varepsilon(\lambda) = S(\lambda, T_{\text{avg}})/S_{\text{BB}}(\lambda, T_{\text{avg}})$.

V. CONCLUSION

In summary, with a combination of a microscope, LIA, and FTIR, we propose and demonstrate a microscopic lock-in FTIR technique, to directly measure the far-field emission of an electrothermal metasurface. The lock-in FTIR is ultrasensitive with a specific detectivity of 8.0×10^{15} Jones that allows us to overcome the heavy optical loss and large background noise during the emission light collection. The microscope subsystem can further reduce the optical loss by a proper optical path alignment together with N_2 purging. With an analysis of the nonlinear signal detection processing from the initial heat generation to the final measured signal output, our method exploits the combination of the global heating and modulated Joule heating for the SNR improvement, achieving a more than 3 times lower temperature to obtain a measurable signal as compared to previous studies. Under a heating temperature of around 125 °C, we can achieve a SNR of about 23.7, which is far above the true-signal-threshold. Furthermore, our system can be applied for a spectral-resolved frequency-domain characterization of the device response and monitor the entire spectra for each modulation frequency. It is expected that our microscopic lock-in FTIR system will become a useful platform for the accurate characterization of modern thermal infrared microdevices.

ACKNOWLEDGMENTS

This work is supported by the Defense Threat Reduction Agency (Grant No. HDTRA1-19-1-0028); National Science Foundation (Grant No. CBET-1931964); ONR DURIP (Grant No. N000142112337).

CONFLICTS OF INTEREST

The authors declare no competing financial interest.

-
- [1] B. Liu, W. Gong, B. Yu, P. Li, and S. Shen, Perfect thermal emission by nanoscale transmission line resonators, *Nano Lett.* **17**, 666 (2017).
 - [2] X. Liu, T. Tyler, T. Starr, A. F. Starr, N. M. Jokerst, and W. J. Padilla, Taming the Blackbody with Infrared Metamaterials as Selective Thermal Emitters, *Phys. Rev. Lett.* **107**, 045901 (2011).
 - [3] Z. Wang, T. S. Luk, Y. Tan, D. Ji, M. Zhou, Q. Gan, and Z. Yu, Tunneling-enabled spectrally selective thermal emitter based on flat metallic films, *Appl. Phys. Lett.* **106**, 101104 (2015).
 - [4] J. Li, Z. Li, X. Liu, S. Maslovski, and S. Shen, Active control of thermal emission by graphene-nanowire coupled plasmonic metasurfaces, *Phys. Rev. B* **106**, 115416 (2022).

- [5] Z. Li, J. Li, X. Liu, H. Salihoglu, and S. Shen, Wiener chaos expansion method for thermal radiation from inhomogeneous structures, *Phys. Rev. B* **104**, 195426 (2021).
- [6] J.-J. Greffet, R. Carminati, K. Joulain, J.-P. Mulet, S. Mainy, and Y. Chen, Coherent emission of light by thermal sources, *Nature* **416**, 6876 (2002).
- [7] A. H. Dorrah, N. A. Rubin, A. Zaidi, M. Tamagnone, and F. Capasso, Metasurface optics for on-demand polarization transformations along the optical path, *Nat. Photonics* **15**, 4 (2021).
- [8] K. Ou, Feilong Yu, Guanhai Li, Wenjuan Wang, Andrey E. Miroschnichenko, Lujun Huang, Peng Wang, Tianxin Li, Zhifeng Li, Xiaoshuang Chen, and Wei Lu, Mid-infrared polarization-controlled broadband achromatic metadvice, *Sci. Adv.* **6**, eabc0711 (2020).
- [9] Z. Yu, N. P. Sergeant, T. Skauli, G. Zhang, H. Wang, and S. Fan, Enhancing far-field thermal emission with thermal extraction, *Nat. Commun.* **4**, 1 (2013).
- [10] Y. Tan, B. Liu, S. Shen, and Z. Yu, Enhancing radiative energy transfer through thermal extraction, *Nanophotonics* **5**, 22 (2016).
- [11] M. Zhou, S. Yi, T. S. Luk, Q. Gan, S. Fan, and Z. Yu, Analog of superradiant emission in thermal emitters, *Phys. Rev. B* **92**, 024302 (2015).
- [12] W. Li and S. Fan, Nanophotonic control of thermal radiation for energy applications [Invited], *Opt. Express* **26**, 15995 (2018).
- [13] D. G. Baranov, Y. Xiao, I. A. Nechepurenko, A. Krasnok, A. Alù, and M. A. Kats, Nanophotonic engineering of far-field thermal emitters, *Nat. Mater.* **18**, 9 (2019).
- [14] Y. Li, W. Li, T. Han, X. Zheng, J. Li, B. Li, S. Fan, and C.-W. Qiu, Transforming heat transfer with thermal metamaterials and devices, *Nat. Rev. Mater.* **6**, 6 (2021).
- [15] M. Zhou, E. Khoram, D. Liu, B. Liu, S. Fan, M. L. Povinelli, and Z. Yu, Self-focused thermal emission and holography realized by mesoscopic thermal emitters, *ACS Photonics* **8**, 497 (2021).
- [16] M. Zhou, H. Song, X. Xu, A. Shahsafi, Y. Qu, Z. Xia, Z. Ma, M. A. Kats, J. Zhu, B. S. Ooi, *et al.*, Vapor condensation with daytime radiative cooling, *Proc. Natl. Acad. Sci. U. S. A.* **118**, e2019292118 (2021).
- [17] L. Zhou, H. Song, J. W. Liang, M. Singer, M. Zhou, E. Stegenburgs, N. Zhang, C. Xu, T. K. Ng, Z. Yu, *et al.*, A polydimethylsiloxane-coated metal structure for all-day radiative cooling, *Nat. Sustainability* **2**, 8 (2019).
- [18] Y. Xiao, A. Shahsafi, C. Wan, P. J. Roney, G. Joe, Z. Yu, J. Salman, and M. A. Kats, Measuring Thermal Emission near Room Temperature Using Fourier-Transform Infrared Spectroscopy, *Phys. Rev. Appl.* **11**, 014026 (2019).
- [19] Y. Xiao, C. Wan, A. Shahsafi, J. Salman, Z. Yu, R. Wambold, H. Mei, B. E. Rubio Perez, W. Derdeyn, C. Yao, M. A. Kats, Precision measurements of temperature-dependent and nonequilibrium thermal emitters, *Laser Photonics Rev.* **14**, 1900443 (2020).
- [20] S. Buddhiraju, A. Song, G. T. Papadakis, and S. Fan, Nonreciprocal Metamaterial Obeying Time-Reversal Symmetry, *Phys. Rev. Lett.* **124**, 257403 (2020).
- [21] B. Zhao, J. Wang, Z. Zhao, C. Guo, Z. Yu, and S. Fan, Nonreciprocal Thermal Emitters Using Metasurfaces with Multiple Diffraction Channels, *Phys. Rev. Appl.* **16**, 064001 (2021).
- [22] K. J. Shayegan, B. Zhao, Y. Kim, S. Fan, and H. A. Atwater, Nonreciprocal infrared absorption via resonant magneto-optical coupling to InAs, *Sci. Adv.* **8**, eabm4308 (2022).
- [23] J. A. Schuller, T. Taubner, and M. L. Brongersma, Optical antenna thermal emitters, *Nat. Photonics* **3**, 11 (2009).
- [24] Y.-Y. Au, H. S. Skulason, S. Ingvarsson, L. J. Klein, and H. F. Hamann, Thermal radiation spectra of individual subwavelength microheaters, *Phys. Rev. B* **78**, 085402 (2008).
- [25] G. Lu, J. R. Nolen, T. G. Folland, M. J. Tadjer, D. G. Walker, and J. D. Caldwell, Narrowband polaritonic thermal emitters driven by waste heat, *ACS Omega* **5**, 10900 (2020).
- [26] Y. De Wilde, F. Formanek, R. Carminati, B. Gralak, P.-A. Lemoine, K. Joulain, J.-P. Mulet, Y. Chen, and J.-J. Greffet, Thermal radiation scanning tunnelling microscopy, *Nature* **444**, 7120 (2006).
- [27] A. C. Jones and M. B. Raschke, Thermal infrared near-field spectroscopy, *Nano Lett.* **12**, 1475 (2012).
- [28] F. Huth, Nano-FTIR nanoscale infrared near-field spectroscopy, <http://purl.org/dc/dcmitype/Text>, Universidad del País Vasco - Euskal Herriko Unibertsitatea, 2015.
- [29] C. Li, V. Krachmalnicoff, P. Bouchon, J. Jaeck, N. Bardou, R. Haïdar, and Y. De Wilde, Near-Field and Far-Field Thermal Emission of an Individual Patch Nanoantenna, *Phys. Rev. Lett.* **121**, 243901 (2018).
- [30] L. Wojszwyk, A. Nguyen, A.-L. Coutrot, C. Zhang, B. Vest, and J.-J. Greffet, An incandescent metasurface for quasimonochromatic polarized mid-wave infrared emission modulated beyond 10 MHz, *Nat. Commun.* **12**, 1 (2021).
- [31] X. Liu, Z. Li, Z. Wang, H. S. Yun, and S. Shen, Design and analysis of electrothermal metasurfaces, *Front. Energy* (2022).
- [32] Y. Yao, R. Shankar, M. A. Kats, Y. Song, J. Kong, M. Loncar, and F. Capasso, Electrically tunable metasurface perfect absorbers for ultrathin mid-infrared optical modulators, *Nano Lett.* **14**, 6526 (2014).
- [33] B. Zeng, Z. Huang, A. Singh, Y. Yao, A. K. Azad, A. D. Mohite, A. J. Taylor, D. R. Smith, and H.-T. Chen, Hybrid graphene metasurfaces for high-speed mid-infrared light modulation and single-pixel imaging, *Light: Sci. Appl.* **7**, 51 (2018).
- [34] R.-J. Shiue, Y. Gao, C. Tan, C. Peng, J. Zheng, D. K. Efetov, Y. D. Kim, J. Hone, and D. Englund, Thermal radiation control from hot graphene electrons coupled to a photonic crystal nanocavity, *Nat. Commun.* **10**, 109 (2019).
- [35] Y. Wang, P. Landreman, D. Schoen, K. Okabe, A. Marshall, U. Celano, H.-S. P. Wong, J. Park, and M. L. Brongersma, Electrical tuning of phase-change antennas and metasurfaces, *Nat. Nanotechnol.* **16**, 6 (2021).
- [36] Y. Zhang, C. Fowler, J. Liang, B. Azhar, M. Y. Shalaginov, S. Deckoff-Jones, S. An, J. B. Chou, C. M. Roberts, V. Liberman, *et al.*, Electrically reconfigurable non-volatile metasurface using low-loss optical phase-change material, *Nat. Nanotechnol.* **16**, 6 (2021).
- [37] S. Abdollahramezani, O. Hemmatyar, M. Taghinejad, H. Taghinejad, A. Krasnok, A. A. Eftekhar, C. Teichrib, S.

- Deshmukh, M. A. El-Sayed, E. Pop, *et al.*, Electrically driven reprogrammable phase-change metasurface reaching 80% efficiency, *Nat. Commun.* **13**, 1 (2022).
- [38] B. Hinkov, F. Pilat, L. Lux, P. L. Souza, M. David, A. Schwaighofer, D. Ristanić, B. Schwarz, H. Detz, A. M. Andrews, *et al.*, A mid-infrared lab-on-a-chip for dynamic reaction monitoring, *Nat. Commun.* **13**, 1 (2022).
- [39] A. Lochbaum, Y. Fedoryshyn, A. Dorodnyy, U. Koch, C. Hafner, and J. Leuthold, On-chip narrowband thermal emitter for mid-ir optical gas sensing, *ACS Photonics* **4**, 1371 (2017).
- [40] D. W. Ball, *Field Guide to Spectroscopy* (SPIE, Bellingham, Wash. (1000 20th St. Bellingham WA 98225-6705 USA), 2006).
- [41] Y. G. Zhang, Y. Gu, K. Wang, X. Fang, A. Z. Li, and K. H. Liu, Fourier transform infrared spectroscopy approach for measurements of photoluminescence and electroluminescence in mid-infrared, *Rev. Sci. Instrum.* **83**, 053106 (2012).
- [42] X. Liu, L. Jing, X. Luo, B. Yu, S. Du, Z. Wang, H. Kim, Y. Zhong, and S. Shen, Electrically driven thermal infrared metasurface with narrowband emission, *Appl. Phys. Lett.* **121**, 131703 (2022).
- [43] Zurich Instruments, Principles of lock-in detection, <https://www.zhinst.com/en/resources/principles-of-lock-in-detection>
- [44] D. A. Skoog, *Principles of Instrumental Analysis*, 7th ed. (Cengage Learning, Australia, 2018).
- [45] P. R. Griffiths and J. A. De Haseth, *Fourier Transform Infrared Spectrometry*, 2nd ed. (Wiley, 2007).
- [46] P. R. Griffiths, “Trading rules” in infrared fourier transform spectroscopy, *Anal. Chem.* **44**, 1909 (1972).
- [47] H. R. Shanks, P. D. Maycock, P. H. Sidles, and G. C. Danielson, Thermal conductivity of silicon from 300 to 1400 K, *Phys. Rev.* **130**, 1743 (1963).
- [48] T. Yamane, N. Nagai, S. Katayama, and M. Todoki, Measurement of thermal conductivity of silicon dioxide thin films using a 3ω method, *J. Appl. Phys.* **91**, 9772 (2002).
- [49] A. Cappella, J.-L. Battaglia, V. Schick, A. Kusiak, A. Lamperti, C. Wiemer, and B. Hay, High temperature thermal conductivity of amorphous Al_2O_3 thin films grown by low temperature ALD, *Adv. Eng. Mater.* **15**, 1046 (2013).
- [50] J. Yang, E. Ziade, and A. J. Schmidt, Uncertainty analysis of thermoreflectance measurements, *Rev. Sci. Instrum.* **87**, 014901 (2016).